Optimization method of CM inductor volume taking into account the magnetic core saturation issues

Bilel Zaidi, Arnaud Videt, Nadir Idir

Optimization method of CM inductor volume taking into account the magnetic core saturation issues

Bilel Zaidi, *Student member, IEEE*, Arnaud Videt, *Member, IEEE,* and Nadir Idir, *Member, IEEE*

***Abstract*—ElectroMagnetic Interferences (EMI) filters are broadly used in power electronic systems in order to respect EMC normative constraints, which considerably increase overall cost and volume mainly because of the common-mode inductor. In this paper, a new method to calculate the optimal volume of the common-mode inductor is proposed. It takes into account core saturation issues that may greatly impact inductor volume and filter performances. Consequently, it is shown that in some cases, increasing the inductance value up to the best value can significantly reduce the filter volume in addition to further enhancing filter attenuation. It is also shown that different nearly-best inductor geometrical parameters with different shape factors can be obtained, which provides an important degree of freedom to designers while introducing the filter in the energy conversion system.**

***Index Terms*—Electromagnetic compatibility standard, Inductor volume design, Magnetic core saturation, Optimization.**

I. Introduction

EMI filters play an important role in power electronic conversion systems. They allow to reduce conducted emissions in order to meet ElectroMagnetic Compatibility (EMC) standards. In fact, switching voltage excites parasitic capacitances naturally existent in the conversion chain and generates conducted electromagnetic interferences with two propagation modes: Differential-Mode (DM) and Common-Mode (CM) disturbances. Using EMI filters, composed of magnetic and capacitive components, allows to these currents to respect EMC standards (e.g DO-160 for aeronautic applications).

In embedded systems, cost, weight and volume of equipments are strong constraints that designers should take into account. As EMI filters usually represent around 30 % of the cost and the volume of the power converters, there is a real need to optimize these passive components, especially the common-mode inductor which occupies the most important part of the EMI filter [1]. Thus, in this paper, studies have been focused on a single-stage common-mode filter, composed of CY capacitors and a coupled CM inductor as shown in Fig. 1. Equivalent capacitance value C_Y of the filter is limited by the maximum current in the capacitor tolerated by electrical safety standards [2]. It is generally set to an application-dependant maximum value. However, the CM inductor volume has to be designed considering not only its inductance value, but also saturation issues caused by inductor voltage V_L (Fig. 2), responsible for flux ripple around the switching frequency [3][4][5][6][7].

B. Zaidi, A. Videt and N. Idir are with Univ. Lille, Arts et Metiers ParisTech, Centrale Lille, HEI, EA 2697 - L2EP - Laboratoire d'Electrotechnique et d'Electronique de Puissance F-59000 Lille, France. e-mail: bilel.zaidi@univ-lille.fr, arnaud.videt@univ-lille.fr, nadir.idir@univ-lille.fr

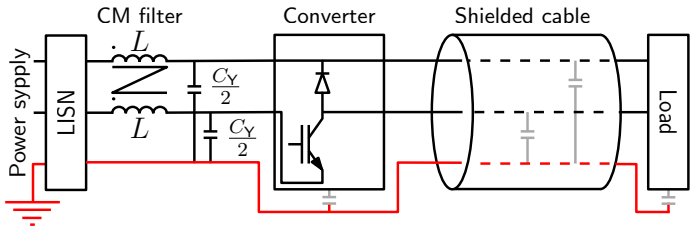

Fig. 1. Considered DC-DC power conversion system.

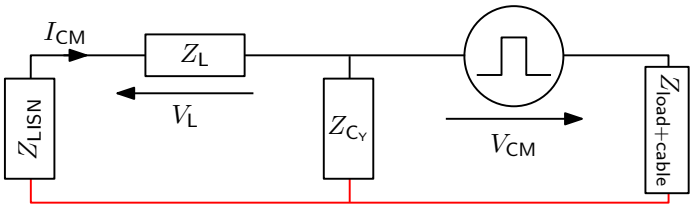

Fig. 2. Simplified CM equivalent circuit of a DC-DC conversion system.

Designing the CM inductor should be performed in two steps. First, the required inductance value L that allows to respect the EMC standard has to be calculated. Many methods existing in the literature allow to determine L value based on the determination of the filter resonance frequency with or without considering the input/output impedances connected to the filter, and with or without taking into account the frequency-dependant complex permeability of the magnetic core [8][9][10][11]. Second, geometric parameters of the magnetic core that allow to obtain L value while respecting saturation constraint must be determined. The "area product" method links magnetic energy, magnetic material saturation flux density and differential current density to the core cross-section multiplied by the window area and the empirically determined window utilization factor [12][13][14]. This method sets a condition to choose the effective magnetic core geometry, but does not propose the optimal geometrical parameters of the magnetic ring core. In [15], a simplified design method of the magnetic core is based on an approximative calculation of its parameters as a function of the number of turns N of the inductor. Other methods based on iterative numerical optimization tools or using private software environments are presented in [1][8][16][17].

In this paper, a new optimization method of toroidal CM inductor volume with considering magnetic core saturation issues is proposed. First, an analytical calculation of the required inductance value is performed taking into account the CM impedances of a DC-DC conversion system and the frequency-dependant complex permeability of the magnetic

material. Second, an optimization tool of CM inductor geometrical parameters taking into account saturation issues is detailed. The third section is dedicated to the application of the proposed method in the design of an EMI filter for a DC-DC conversion system. Simulation results will be validated with experimental data in the last part of the paper.

II. Optimal Design of the Common-Mode Inductor

A. Detemination of the minimal required inductance value

A simplified common-mode model of the DC-DC conversion system is presented in Fig. 2. The CM source of this system is considered as a trapezoidal signal with a magnitude equal to the half of DC supply voltage. This model takes into account many important parameters: 1) The LISN impedance that notably includes a resonance (low impedance) in low frequencies (before 150 kHz) that may increase the maximum common-mode current involved in saturation issues [4]. In fact, common-mode core saturation phenomenon is principally impacted by the CM currents in low frequencies (around switching frequency). If the CM LISN impedance was considered as a 25 Ω resistance (ideally two 50-ohm resistors in parallel) for the calculation of the CM current, then the maximum CM current and the correspondent maximum magnetic field would be underestimated which may induce an error in the design of the CM inductor. 2) The load and the shielded cable CM impedances that contain resonances in high frequencies (beyond 150 kHz). 3) Parasitic elements ESL and ESR of the equivalent capacitance C_Y. 4) The frequency-dependant complex permeability $\overline{\mu}_r$. In this study, the magnetic material is chosen beforehand. Thus, $\overline{\mu}_r$ is an input parameter. Parasitic capacitances to the ground of the DC-DC converter and inter-turns capacitances of the coupled CM inductor are not included in this model. These elements may have an impact on the filter performance in the MHz frequencies, which reduces the accuracy of the used model to a frequency range that can be extended to at least 2 MHz as it will be shown in the last section of the paper. In fact, the purpose of this paper is to show the impact of saturation issues around the switching frequency on the CM inductor volume. Thus, the objective is to design a CM filter that allows to respect the EMC standard in the frequency range between 150 kHz and 2 MHz.

From the CM equivalent circuit of Fig. 2, CM current I_{cm} can be analytically determined as a function of V_{CM}, Z_{LISN}, $Z_{load+cable}$, Z_{C_Y} and Z_L as shown in eq. (1). However, in order to take in consideration the effect of the complex permeability and the geometry of the toroidal magnetic core in the calculation process, Z_L is replaced by eq. (2). Then, solving the inequality of eq. (1) is performed in all the frequency range between 150 kHz and 2 MHz. For a given filter equivalent capacitance value C_Y, it determines minimal value of a geometrical parameter A of the magnetic core for each frequency. The design frequency of the minimal required inductance value L_{LF}^{min} is defined as the frequency where the CM current with filter touches the standard limit as shown in Fig. 3. Then, L_{LF}^{min} will be deduced at a chosen reference frequency (e.g 1 kHz in eq. (2)), where LF stands for "Low Frequency",

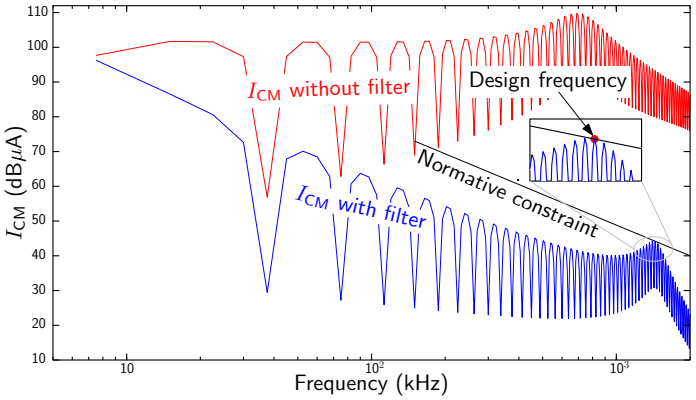

Fig. 3. CM current evolution with and without filter.

arbitrarily chosen to normalize the given inductance values that depend on frequency due to $\overline{\mu}_r(f)$. Thus, L_{LF}^{min} is a boundary such that larger inductance values ($L_{LF} \geq L_{LF}^{min}$) allow to respect the standard with extra attenuation (even if not necessary), while lower inductance values are not sufficient. Fig. 4 presents this boundary by repeating the process for several capacitance values. In this figure, L_{LF}^{min} evolution and the corresponding design frequency as a function of C_Y are plotted for an example of a nanocrystalline magnetic material (system components and parameters will be further detailed in section III). As shown in Fig. 4, increasing C_Y decreases not only L_{LF}^{min} but also the design frequency. The latter is strongly impacted by the cable first resonance and the C_Y value which slightly shifts the "apparent" resonance frequency of I_{cm} to low frequencies (Z_{C_Y} is in parallel with $Z_{load+cable}$ in the equivalent Thevenin circuit of Fig. 2). Knowing the required inductance value, a new proposed method allows to determine optimal geometrical parameters of the magnetic core that minimizes its volume. Note that results presented in figures 3 and 4 correspond to an example for a given converter duty cycle D. When the CM filter design should be effective for the worst case duty cycle value, the presented calculation process should be performed for $D = 50\,\%$ which updates the V_{CM} spectrum in eq. (1) as explained in [5].

$$\begin{cases} I_{cm}(f) = \dfrac{Z_{C_Y}}{Z_{C_Y}.(Z_{LISN}+Z_L)+Z_{load+cable}.(Z_{C_Y}+Z_L+Z_{LISN})} V_{CM}(f) \\ \\ |I_{cm}(f)| \leqslant \textit{EMC Standard level} \quad \forall \quad 150\,\text{kHz} \leqslant f \leqslant 2\,\text{MHz} \end{cases} \tag{1}$$

$$\begin{cases} Z_L = j2\pi f.\overline{\mu}_r(f).A \\ \overline{\mu}_r = \mu_r' - j\mu_r'' \\ A = \mu_0.N^2.\frac{h}{2\pi}\ln(\frac{R}{r}) \\ \mu_r = \mu_r'(1\,\text{kHz}) \\ L_{LF} = \mu_r.A \end{cases} \tag{2}$$

It is noteworthy that the L_{LF}^{min} versus C_Y drawn in log-log scale in Fig. 4 is not a straight line, indicating that the filter "resonance frequency" depends on the selected C_Y value. Thus, analytical calculation based on eq. (1) and eq. (2) are more accurate than methods relying only on filter resonance determination [10], especially due to taking into account the input/output impedances connected to the filter in addition to

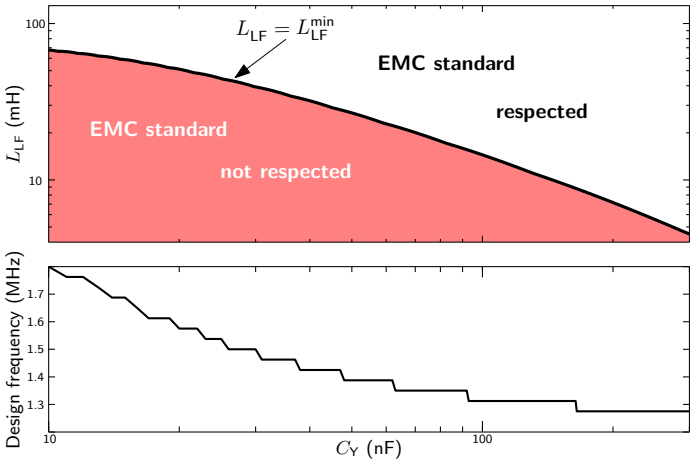

Fig. 4. Minimal required inductance value L_{LF}^{min} and the corresponding design frequency versus C_Y values.

the frequency-dependant complex permeability.

B. Optimal geometrical parameters determination of the CM coupled inductor

The common-mode inductor is composed of two windings coupled on the same magnetic core and wound in the same direction as shown in Fig. 5. Then, the magnetic material is ideally not impacted by the differential current of the system. Global volume V of the CM inductor in eq. (3) depends on external radius R, the height h and wire diameter d, which is determined depending on the differential current and the tolerated current density in the system. For a given inductance value L_{LF} and relative permeability μ_r, A depends on the height h, the external radius R, the number of turns N and the internal radius r as shown in eq. (2). Thus, h can be expressed as a function of these parameters and the required inductance value, such that V becomes a function of three variable parameters: R, r and N. Reducing the number of parameters of V will help to find optimal geometrical parameters R, r, h and N of the inductor. This can be achieved by ensuring two constraints used to guarantee the best performance of the inductor. The first one, named NS for "Non Saturation", ensures that the magnetic material will not saturate by verifying that the maximum magnetic field H_{max} in the inductor is lower than the saturation magnetic field H_{sat} of the used material as shown in eq. (4). This constraint sets a lower bound of the internal radius r, named r_{min1}, that only depends on N. The second constraint, named SL for "Single Layer", sets the number of layers of the inductor to one as shown in eq. (5), where s is the inter-turn minimum spacing as defined in Fig. 5. In fact, previous studies have shown that constructing a choke with only one layer greatly reduces parasitic capacitance of the inductor [18]. This constraint sets another lower bound of r, named r_{min2}, that only depends on N too. NS and SL constraints and their resulting lower bounds, r_{min1} and r_{min2} are detailed in Tab. I. Designing a toroidal inductor with the minimal volume naturally needs the lowest internal radius. For this reason, in the following, depending on the ensured constraint, internal radius r will be equal to r_{min1}

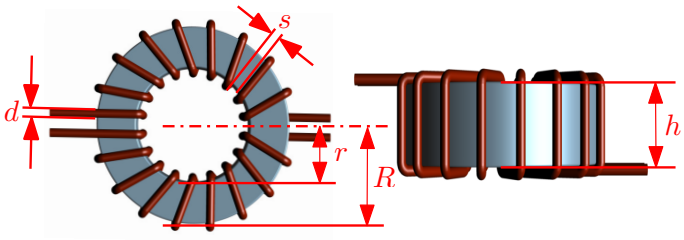

Fig. 5. Geometrical parameters of the common-mode inductor.

TABLE I
CONSTRAINTS TO AVOID MULTIPLE LAYERS AND MAGNETIC SATURATION.

Constraint	condition	$r_{min1,2} = K_1 N + K_2$
NS: Non Saturation	$r \geq \frac{I_{max}}{2\pi H_{sat}} N \quad (= r_{min2})$	$K_1 = \frac{I_{max}}{2\pi H_{sat}} \quad K_2 = 0$
SL: Single Layer	$r \geq \frac{d+s}{\pi} N + \frac{d}{2} \quad (= r_{min1})$	$K_1 = \frac{d+s}{\pi} \quad K_2 = \frac{d}{2}$

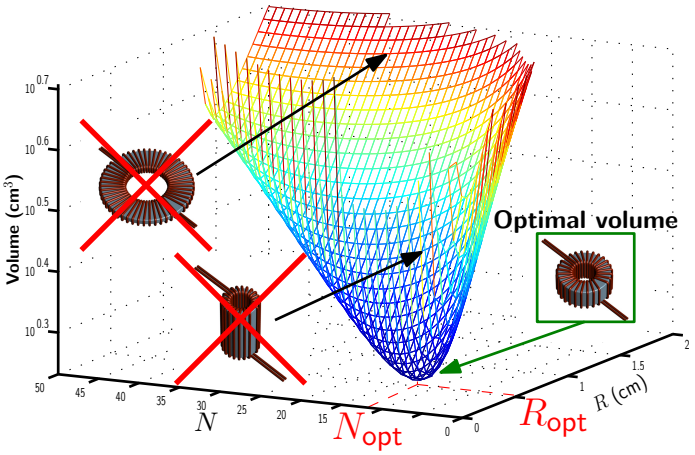

Fig. 6. Inductor volume example versus R and N for the same L_{LF} value.

or r_{min2}, and will be function of only the number of turns N ($r = K_1 N + K_2$ as shown in Tab. I). Thus, inductor volume V depends on only two variable parameters: N and R as shown in eq. (6). For a given inductance value L_{LF}, inductor volume is presented as a function of N and R in Fig. 6. This curve clearly shows the existence of an optimal (R_{opt}, N_{opt}) that optimises V. This point can be numerically obtained by solving the intersection between the derivatives of V with respect to R and N as detailed in eq. (7) ($\frac{\partial V}{\partial R}|_{N_{opt}} = \frac{\partial V}{\partial N}|_{R_{opt}} = 0$).

$$V = \pi(h + 2d)(R + d)^2. \tag{3}$$

$$H_{max} = \frac{N I_{max}}{2\pi r} \leqslant H_{sat}. \tag{4}$$

$$2\pi\left(r - \frac{d}{2}\right) \geqslant 2N\,(d + s)\,. \tag{5}$$

$$V(R, N) = \pi\left(\frac{2\pi L_{LF}}{\mu_0 \mu_r N^2 \ln\left(\frac{R}{K_1 N + K_2}\right)} + 2d\right)(R + d)^2\,. \tag{6}$$

$$\begin{cases} R_{\text{opt}} = \left(K_1 N_{\text{opt}} + K_2\right) \exp\left(\frac{K_1 N_{\text{opt}}}{2\left(K_1 N_{\text{opt}}+K_2\right)}\right) \\ \ln^2\left(\frac{R_{\text{opt}}}{K_1 N_{\text{opt}}+K_2}\right) + \frac{\pi L_{\text{LF}}}{\mu_0 \mu_r d N_{\text{opt}}^2} \ln\left(\frac{R_{\text{opt}}}{K_1 N_{\text{opt}}+K_2}\right) - \frac{\pi L_{\text{LF}}}{2\mu_0 \mu_r N_{\text{opt}}^2}\left(\frac{1}{d} + \frac{1}{R_{\text{opt}}}\right) = 0. \end{cases} \tag{7}$$

The flowchart of the proposed method, presented in Fig. 7, is composed of two principal parts: "Input Parameters" and "Optimal Inductor Volume Calculation" parts. In the first one, as the magnetic material characteristics (H_{sat} and $\overline{\mu}_r$) are chosen beforehand and as CM model elements are known (V_{CM}, Z_{LISN} and $Z_{\text{load+cable}}$), minimal required inductance values $L_{\text{LF}}^{\text{min}}$ to meet the normative constraint are calculated for each equivalent capacitance value C_{Y}. Then, for a given allowed (L_{LF}, C_{Y}), computation of the time-dependant common-mode current can be performed by IFFT of the calculated I_{cm} in eq. (1) and its maximum value I_{max} can be easily determined. Wire diameter d is set to a constant value depending on the differential current. The last input parameter, minimal wire spacing s, is freely set to a constant value to possibly reduce inter-turn parasitic capacitance. All these parameters will be used in the second part of the proposed flowchart.

The "Optimal Inductor Volume Calculation" part is based on the resolution of the system of equations of eq. (7) each time a constraint is ensured. To start with, the single-layer constraint SL is ensured by selecting $K1$ and $K2$ in Tab. I so as to set $r = r_{\text{min}1}$. Thus, geometrical parameters (R_{opt} and N_{opt} of Fig. 6) are calculated to obtain optimal inductor volume without considering the common-mode current impact on the the magnetic material. Then, in the second step, the non saturation constraint NS is checked by comparing the obtained H_{max} from the first calculation to the magnetic core H_{sat}. If the NS constraint is respected, then the precess is ended and the optimal CM inductor geometry (R_{opt}, r_{opt}, h_{opt} and N_{opt}) is obtained. If not, the process continues by ensuring the second constraint NS ($r = r_{\text{min}2}$ in Tab. I). This constraint naturally decreases the number of turns N_{opt} in order to set H_{max} equal to H_{sat} and increases the inductor height h_{opt} constrained by the inductor value L_{LF}, which tends to increase the inductor volume and makes the SL constraint satisfied in most cases. However, if needed, the process can ensure both SL and NS constraints by solving eq. (8), which determines an optimal number of turns N_{opt}, and a resulting R_{opt} can be obtained with the second equation of the system in eq. (7) ($\frac{\partial V}{\partial R}|_{N_{\text{opt}}} = 0$).

$$\frac{s+d}{\pi} N + \frac{d}{2} = \frac{I_{\text{max}}}{2\pi H_{\text{sat}}} N. \tag{8}$$

It will be shown later that when both SL and NS constraints are ensured, "nearly-best" inductor volume can be obtained with different core geometries, which provides an extra degree of freedom to designers while determining the global design of the converter. In the next part of the paper, the proposed method will be validated with simulations and experimentations.

III. Validation of the Proposed Method with Simulations

Simulations were performed with the system of Fig. 1. The DC-DC converter is powered by a DC source of 540 V and commutes at a switching frequency F_{s} equal to 7.5 kHz with a duty cycle D equal to 20 %. It should be noticed that this duty cycle value does not correspond to the maximum CM current situation: as shown in [5], common mode current is maximal for 50 % duty cycle so that designing a CM filter for applications where duty cycle may take any value should be performed for D equal to 50 %. Thus, the following designs are only valid for 20 % duty cycles, which will ease experimental validations in section IV regarding saturation effects.

An R-L load is connected to the converter through a 28-meter shielded cable with a CM impedance $Z_{\text{load+cable}}$ presented in Fig. 8 (black curve). The considered EMC standard is the aeronautic D0-160 catogory B. Thus, the used LISN is the NNBM 8126-A with a CM impedance presented in Fig. 8 (red curve). The used magnetic material is a nanocrystalline from APERAM manufacturer with a high saturation flux density B_{sat} equal to 1.2 T and μ_{r} equal to 126000. Its complex permeability evolution with frequency is measured and presented in Fig. 9. An equivalent saturation magnetic field H_{sat} is defined in eq. (9). Note that in the calculation process, a security margin of 25 % of B_{sat} is taken into account. In practical use, it may be wise to secure a larger margin to take into account possible dispersion in the material characteristics and ensure that saturation is always avoided. In this paper, the material is known from laboratory characterizations, and a reasonable margin is affordable so that experiments can easily verify when cores are close to saturation.

$$H_{\text{sat}} = \alpha \frac{B_{\text{sat}}}{\mu_0 \mu_r'(F_{\text{s}})} \quad ; \quad \alpha = 0.75. \tag{9}$$

The last two input parameters of the proposed flowchart in figure 7 are the wire diameter d and the minimal wire spacing s. The latter is arbitrarily chosen equal to 0.1 mm and the wire diameter d is set equal to 0.8 mm depending on the differential current value.

A. Minimal inductance value versus best inductor volume

Minimal inductance values $L_{\text{LF}}^{\text{min}}$ are calculated for several C_{Y} equivalent capacitance values between 10 nF and 300 nF and presented in Fig. 10 using the proposed method detailed in section II-A. Then, optimal inductor volume is calculated for each $L_{\text{LF}}^{\text{min}}$ using the flowchart of Fig. 7 and the obtained result is presented in Fig. 11. As expected, increasing C_{Y} values decreases inductor volume. However, for these inductance values ($L_{\text{LF}}^{\text{min}}$), CM current around the switching frequency F_{s} is high, which induces saturation issues in the magnetic material. For this reason, the optimization process has to ensure the non saturation constraint NS, which reduces the number of turns N_{opt} (comparing to the calculation process with SL constraint) and calculates an optimal geometry (R_{opt}, r_{opt}, h_{opt}) that leads to a big inductor volume.

It is worth noting that even though $L_{\text{LF}}^{\text{min}}$ is determined based on the normative constraint above 150 kHz, saturation

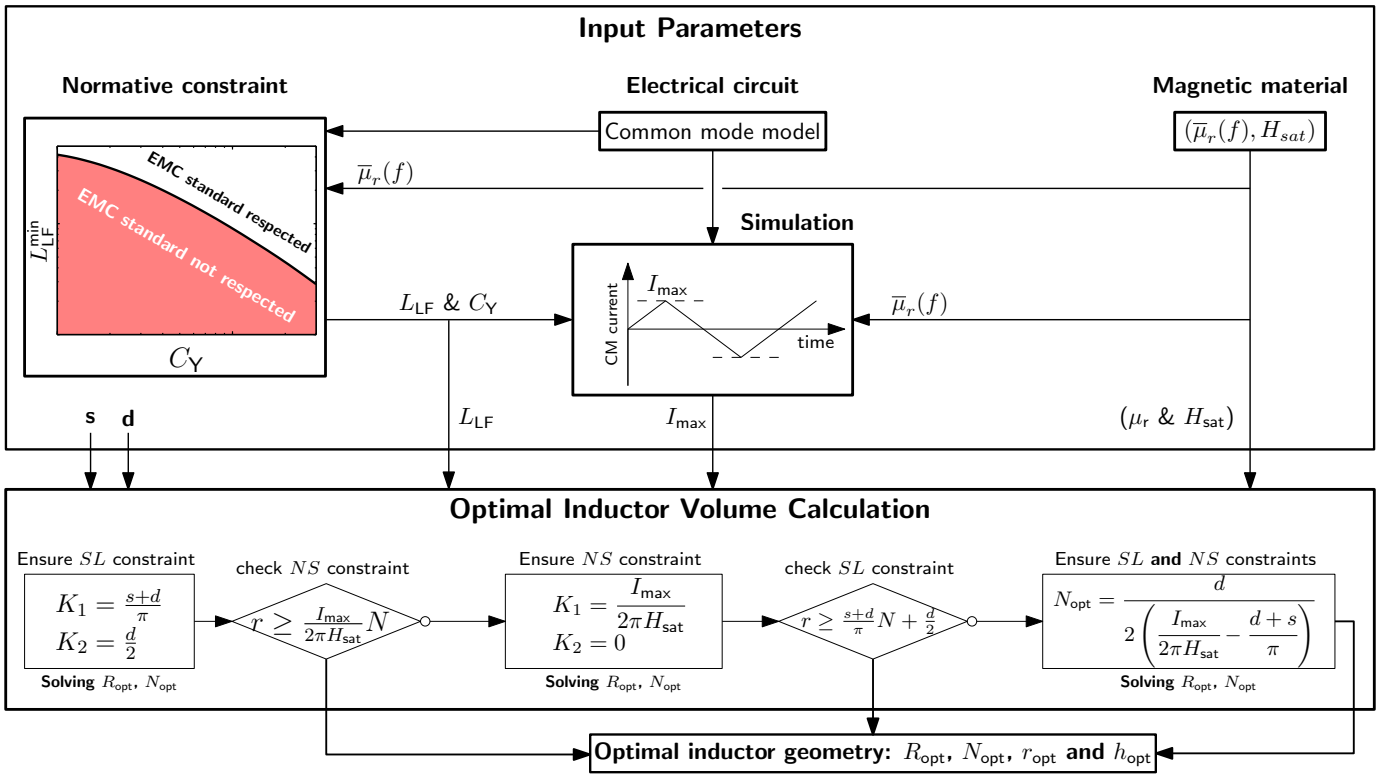

Fig. 7. Flow chart of the proposed CM inductor design method.

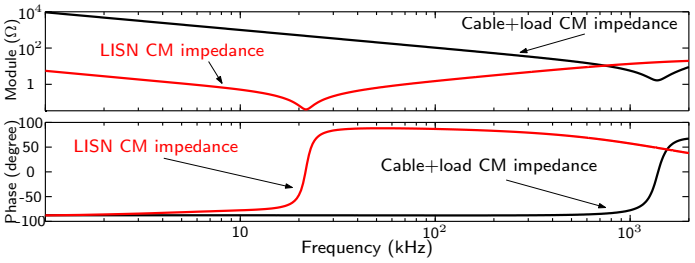

Fig. 8. CM impedances of the used LISN and shielded cable + load.

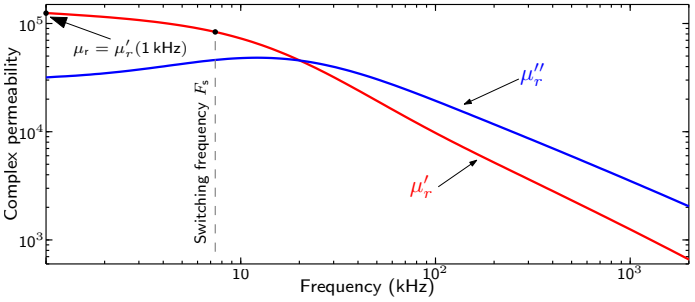

Fig. 9. Complex permeability versus frequency of the nanocrystalline material.

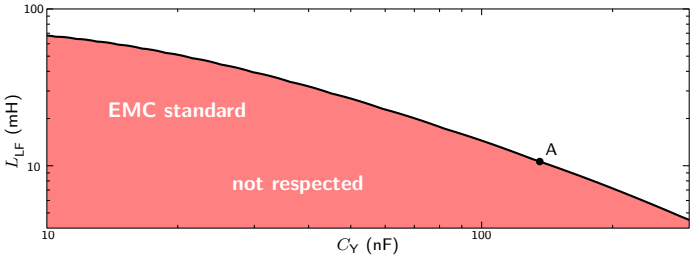

Fig. 10. Minimal inductance values evolution versus C_Y.

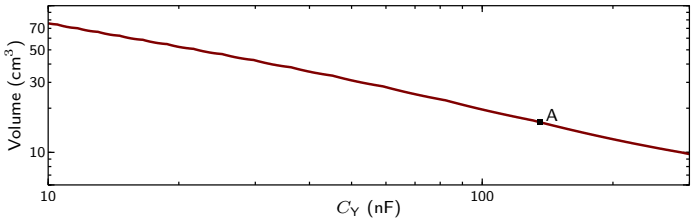

Fig. 11. Optimal inductor volume for minimal inductance values versus C_Y.

appears due to magnetic field ripple at the switching frequency (7.5 kHz) and impacts filter performances beyond 150 kHz as well, as will be shown in experimental results.

Increasing inductance value L_{LF} higher than L_{LF}^{min} not only improves the CM filter attenuation, but also allows to decrease CM current in low frequencies, as shown in Fig. 12 for a given capacitance value C_Y, equal to 136 nF, and may reduces CM current impact on the inductor geometry. When C_Y = 136 nF (two capacitors of 68 nF), its corresponding minimal required inductance value L_{LF}^{min} is equal to 10.7 mH at point A of Fig. 10 (optimal inductor volume equal to 15.9 cm^3 in Fig. 11). Then, beginning from this point and using the optimization tool of Fig. 7, optimal inductor volume values are calculated for several allowed inductance values ($L_{LF} \geqslant L_{LF}^{min}$) and are presented in Fig. 13.

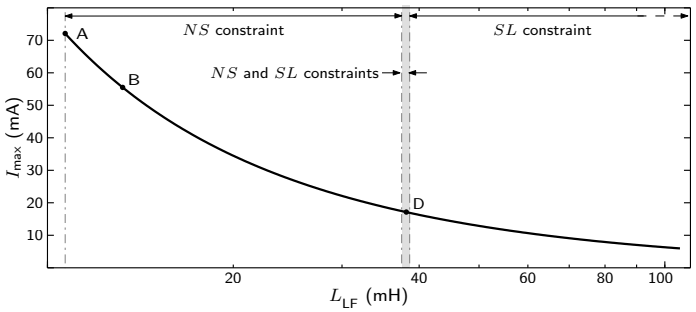

Fig. 12. Maximum CM current I_{max} versus L_{LF} for C_Y = 136 nF.

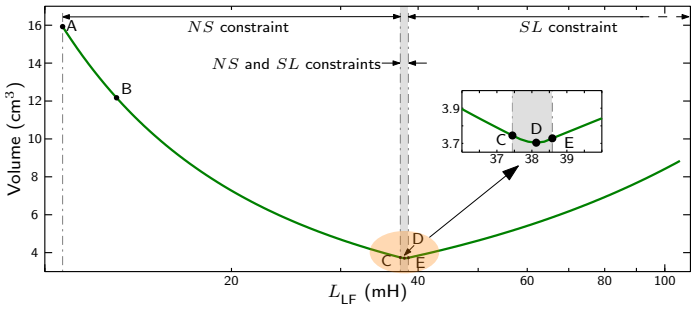

Fig. 13. Optimal inductor volume evolution versus L_{LF} for C_Y = 136 nF.

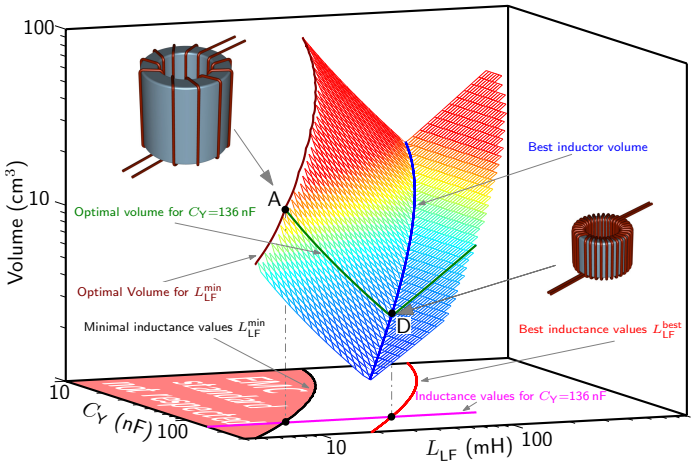

Fig. 14. Optimal inductor volume evolution versus allowed L_{LF} and C_Y.

As expected, increasing L_{LF} decreases optimal inductor volume. But the *NS* constraint is still ensured up to point C in Fig. 13, in which both *NS* and *SL* constraints start to be ensured while calculating optimal inductor volume. Between points C and E of Fig. 13, *NS* and *SL* constraints are ensured at the same time. In this interval, best inductance value L_{LF}^{best} that minimises the optimal inductor volume is determined at point D. Its value 38.12 mH is almost four times L_{LF}^{min} however its inductor volume equal to 3.71 cm^3 yields more than 75 % reduction of the optimal inductor volume at point A. Beyond point E, there is no need to ensure the non saturation constraint *NS* and inductor volume is calculated by only ensuring the single layer constraint *SL*. Then, increasing L_{LF} value increases the number of turns N_{opt} and naturally increases optimal inductor volume as shown in Fig. 13. Thus, for this equivalent

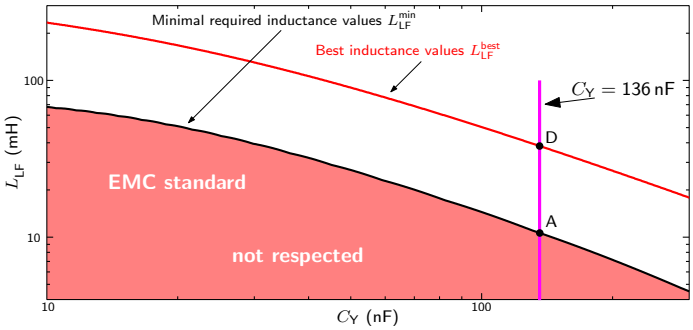

Fig. 15. Minimal and best inductance values evolution versus C_Y.

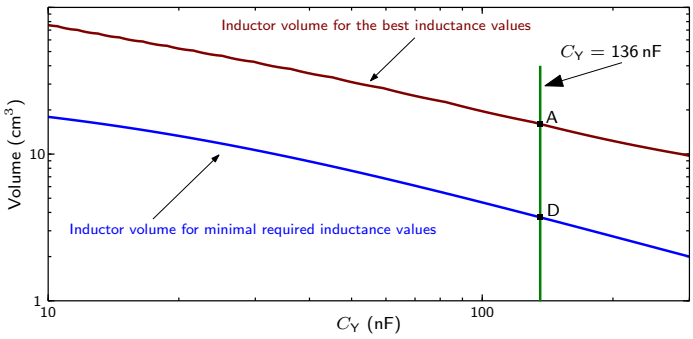

Fig. 16. Optimal inductor volumes for minimal and best inductance values.

capacitance value (C_Y = 136 nF), best inductor volume is not obtained at L_{LF}^{min} but at the larger inductance value L_{LF}^{best}. For this reason, optimal inductor volume calculation process was performed for several allowed inductance values L_{LF} and for several equivalent capacitance values C_Y between 10 nF and 300 nF and is drawn in Fig. 14.

For all the considered capacitor values, best inductance values L_{LF}^{best} that optimise inductor volume are higher than L_{LF}^{min} in the whole 3D curve of Fig. 14 as shown in Fig. 15 (red line). The correspondent best inductor volume presented in Fig. 16 (blue line) shows how the increase of L_{LF} up to L_{LF}^{best} can considerably reduce the inductor volume compared to the L_{LF}^{min} inductor volume. The inductor volume reducing is related to the I_{max} evolution which decreases with L_{LF} up to a point where *NS* constraint is no longer the limiting factor to volume reduction as shown in Fig. 12. Generally, when inductor volume is designed by ensuring the non saturation constraint, it is more reasonable to increase inductance value up to L_{LF}^{best} in order to optimize its volume.

Best inductance values presented in Fig. 15 decrease with equivalent capacitance value C_Y from more than 200 mH to 20 mH, which may seem to be huge values. However, the presented inductance values are calculated at 1 kHz as explained in section II-A and the used magnetic material relative permeability rapidly decreases with frequency as shown in Fig 9. Then, for example, for the best inductance value in point D (38.12 mH), its value at 150 kHz is only about 2 mH.

For each equivalent capacitance value C_Y in Fig. 15, best inductance value L_{LF}^{best} is greatly higher than L_{LF}^{min}. Since this increases filter attenuation and provides some margin to respect the standard, it might be expected that the increasing of

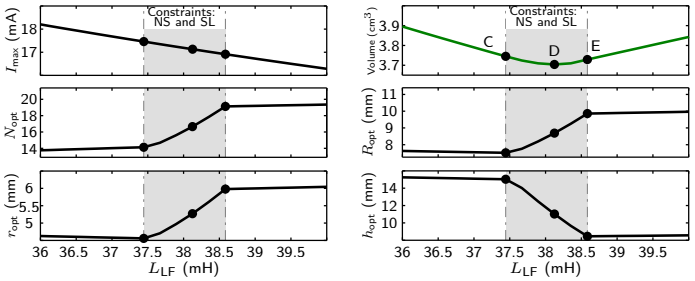

Fig. 17. Optimal geometric parameters evolution when both SL and NS constraints are ensured for C_Y = 136 nF.

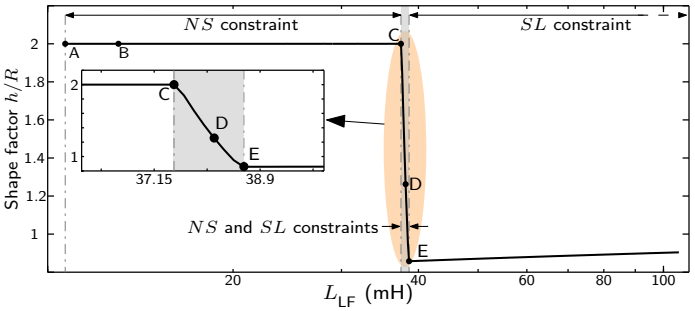

Fig. 18. Shape factor versus L_{LF} for C_Y = 136 nF.

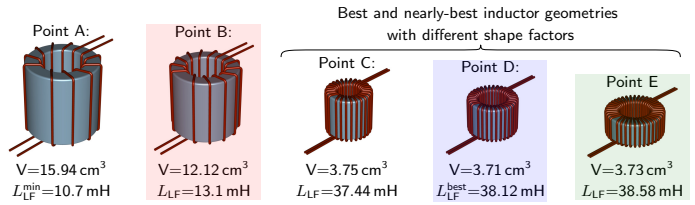

Fig. 19. Different inductor geometries at points A, B, C, D and E (same scale).

L_{LF} could allow to reduce the C_Y value. However, decreasing the equivalent capacitance value increases the common-mode current and constraints the design of the CM inductor by the NS constraint which can be avoided only by increasing the best inductance value as shown in Fig. 15 (C_Y decreases from 300 nF to 10 nF). Thus, decreasing the C_Y value is penalized by the increasing of L_{LF}^{best} and the correspondent best volume as shown in Fig 16.

For inductance values between C and E in Fig. 13, inductor volume is almost equal to its best value. It will be shown in the next section that there are several possible "nearly-best" inductor geometries with quite different shapes for almost the same L_{LF}^{best} and the same best inductor volume.

B. Best inductor geometries

Inductance values between points C and E in Fig. 13 present a transition between the two ensured constraints NS and SL while calculating optimal inductor volume. In this interval, L_{LF} and its optimal volume are almost the same (37.44 mH $\leqslant L_{LF} \leqslant$ 38.58 mH while 3.71 cm^3 $\leqslant V \leqslant$ 3.75 cm^3). Then, as shown in eq. (10), which is only valid between points C and E where both NS and SL constraints are ensured, all geometrical parameters of the inductor are function of I_{max} which continues to decrease even slightly as shown in Fig. 17 (h_{opt} increases with I_{max} while N_{opt}, r_{opt} and R_{opt} decrease).

$$\begin{cases} N_{opt} = \dfrac{d}{2\left(\frac{I_{max}}{2\pi H_{sat}} - \frac{d+s}{\pi}\right)} \\ r_{opt} = \dfrac{dI_{max}}{2I_{max} - 4H_{sat}(d+s)} \\ R_{opt} \approx \dfrac{dI_{max}}{2I_{max} - 4H_{sat}(d+s)} \exp\left(\frac{1}{2}\right) = r_{opt}\exp\left(\frac{1}{2}\right) \\ h_{opt} \approx \dfrac{16L_{LF}\left(\frac{I_{max}}{2H_{sat}} - d - s\right)^2}{\mu_0\mu_r\pi d^2} \end{cases} \quad (10)$$

Optimal inductor volume and its optimal geometrical parameters variations are drawn in Fig. 17 when L_{LF} is between C and E points. For almost the same inductor value and volume, optimal geometrical parameters can completely change from a small R_{opt} (7.52 mm) with a large h_{opt} (15.03 mm) at point C to a larger R_{opt} (9.86 mm) and a much smaller h_{opt} (8.45 mm) at point E. Thus, the shape factor of the core dimensions $\frac{h}{R}$, drawn in Fig. 18, continuously decreases by a factor of 2.3 between points C and E. In fact, solving eq. (7) when the NS constraint is ensured shows that the optimal height h_{opt} is always equal to the double of the optimal external radius R_{opt} ($h_{opt} = 2R_{opt}$). However, when the SL constraint starts to be ensured, h_{opt} becomes lower than R_{opt} ($h_{opt} = 0.86R_{opt}$ at point E in Fig. 18). The best and nearly-best geometries at points C, D, and E are presented in Fig. 19. We note that the difference between the three volumes is lower than 2 %. Interestingly, as shown in Fig. 18, the shape factor variation is quite steep between points C and E, which span a tight range of inductance values. In comparison, for lower inductance values, the shape factor curve is flat ($\frac{h}{R}$ is equal to 2 between points A and C) and for higher L_{LF} values $\frac{h}{R}$ slowly increases (above point E in Fig. 17 and Fig. 18).

Thus, depending on other design constraints (e.g core surface for thermal exchange, core weight, free place in the converter...), designers have the choice between several optimal geometrical parameters while guaranteeing about the same optimal volume of the inductor. In comparison, optimal inductor volumes for lower inductance values (at point A in Fig. 13 at L_{LF}^{min} and point B at $L_{LF} > L_{LF}^{min}$) are also presented in Fig. 19 with the same scale.

The fast change of parameters between points C and E can be explained by considering Fig 20 which presents relationships between r and N depending on I_{max} value, and thereby on inductance value according to Fig.12. Indeed, Tab. I and section II.B show that r can be written as an affine function of N: $r = r_{min1}(N)$ or $r = r_{min2}(N)$, with the constraint that it cannot be inferior to either of these two expressions. Thus, Fig 20 presents $r = r_{min1}(N)$ straight blue line as non varying because both the slope and the $N = 0$ intercept point are related to constant parameters (d and s) in Tab. I. However, the $r = r_{min2}(N)$ red line is a linear function of which the slope is proportional to I_{max}. Therefore, the slope decreases in the examples of Fig 20 (a) to (c) as a result of increasing

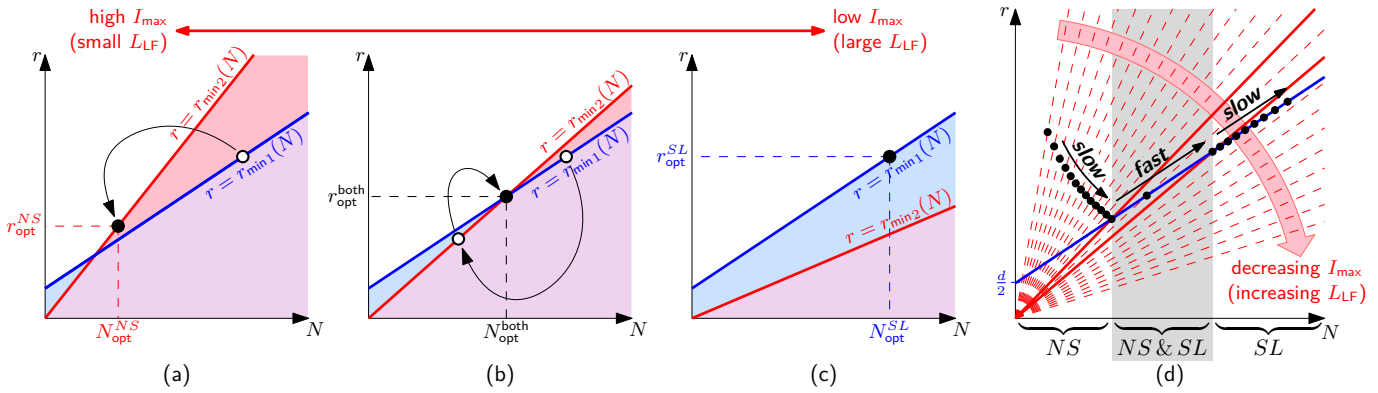

Fig. 20. Different steps of the inductor volume for each inductance value.

L_{LF}, which decreases I_{max}.

The algorithm in Fig 7 starts by setting $r = r_{min1}(N)$ to ensure SL constraint and then finds the optimal geometrical parameters including r_{opt}^{SL} and N_{opt}^{SL}. If L_{LF} is large enough (Fig 20(c)), then the result (black circle) places r_{opt}^{SL} above $r_{min2}(N_{opt}^{SL})$, which naturally fulfills the NS constraint and terminates the algorithm.

On the contrary, if L_{LF} is small (Fig 20(a)), then the result (white circle) may not respect the NS constraint as it is located below the $r_{min2}(N)$ curve. Therefore the algorithm (Fig 7) continues by setting $r_{min2}(N)$ to ensure NS constraint, and new optimal parameters r_{opt}^{NS} and N_{opt}^{NS} are determined. If this result (black circle in Fig 20(a)) places r_{opt}^{NS} above $r_{min1}(N_{opt}^{NS})$, then SL constraint is naturally respected and the algorithm terminates. Otherwise (Fig 20(b)), both SL and NS constraints must be enforced at once, which determines r_{opt}^{both} and N_{opt}^{both} at the $r_{min1}(N)$ and $r_{min2}(N)$ intercept point. Such situation happens as a transition between the two preceding cases with intermediate L_{LF} values.

The last situation is the one that happens between points C and E in Figs. 17 and 18. Since $r_{min1}(N = 0)$ equals $\frac{d}{2}$ which is much smaller than the internal radius r_{opt}^{both}, the two straight lines become near parallel, such that their intercept point rapidly varies even with slight variation of the L_{LF} value. This effect is illustrated in Fig 20(d) where the optimal point quickly moves in the region where both NS and SL constraints are ensured, which explains the steep parameters variations between points C and E. Equation (10) actually applies only in this region. Thus, this tight interval [C, E] can be exploited to construct many inductors with different shape factors for almost the same inductance value.

Inductor weight evolution with L_{LF} can be deduced from the inductor iron volume V_{iron} defined in eq. (11) and plotted in Fig. 21(a). Its evolution shows that best V_{iron} is obtained in the [C E] interval at point E with a slight difference of 1.2 % from V_{iron} value at point D.

$$V_{iron} = \pi(R_{opt}^2 - r_{opt}^2)h_{opt}. \tag{11}$$

Core surface S_{core}, calculated using eq. (12), is also an important parameter that defines the ability of the magnetic core to be naturally cooled, as larger S_{core} provides larger heat exchange surface with ambient air.

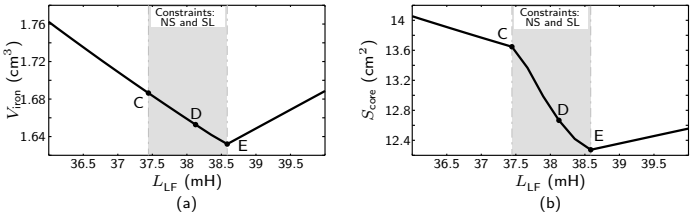

Fig. 21. V_{iron} and S_{core} evolution versus L_{LF} between points C and E for C_Y = 136 nF.

$$S_{core} = 2\pi(R_{opt}^2 - r_{opt}^2) + 2\pi(R_{opt} + r_{opt})h_{opt}. \tag{12}$$

Results obtained in Fig. 21(b) show that, in [C E] interval, best core surface S_{core} is obtained at point C. Increasing L_{LF} to point E, S_{core} looses about 10 % from its best surface at point C. Thus, between different application constraints, designer can choose the best geometry from best inductors calculated with the proposed method.

IV. Experimental Validation of the Proposed Method

To validate the proposed method, measurements were performed with the experimental set-up of Fig. 22 which is the same presented in the previous section. Notably, the target duty cycle is still 20 %, which means that realized filters are expected to meet the standard at this value and may fail if duty cycle is changed in such a way that magnetic flux increase up to core saturation. Observing this feature will allow to verify whether the realized inductors operate near saturation in the following. Three different CM filters with three CM inductors chosen from Fig. 19 and presented in Fig. 23 were used to validate the proposed method using a nanocrystalline material. Their calculated optimal geometrical parameters and the physically realized devices are presented in Tab. II. Each one of the used capacitors of 68 nF can support a maximal AC voltage of 275 V which is larger than the CM voltage harmonics and has a volume of 0.85 cm^3.

The used model correctly predict the CM current without filter even beyond 2 MHz as shown in Fig. 24 (gray line for the model and dark red line for the experiment). In fact, the

TABLE II
INDUCTORS CHARACTERISTICS.

Inductors	B	D	E
Inductance value L_{LF} (mH)	13.1	38.12	38.58
Optimal number of turns N_{opt}	7	17	20
Calculated (R_{opt}, r_{opt}, h_{opt}) (mm)	(11.55, 7, 23.1)	(8.7, 5.27, 11.02)	(9.86, 5.98, 8.45)
Used (R_{opt}, r_{opt}, h_{opt}) (mm)	(12.5, 8, 20)	(8, 5, 12)	(10, 6.25, 8)
Minimal wire spacing s (mm)	0.1		
Wire section (mm^2)	0.5		

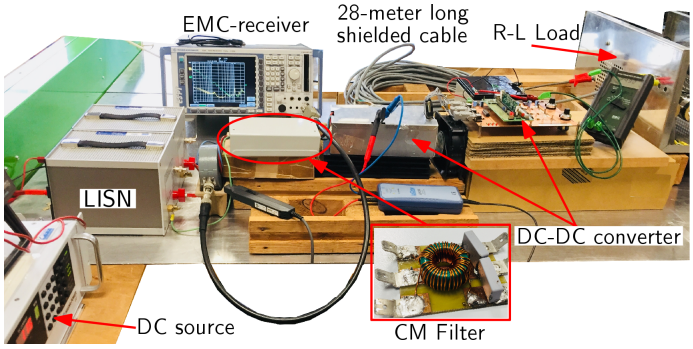

Fig. 22. Experimental set-up.

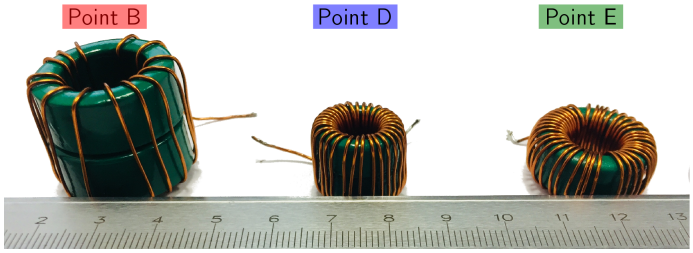

Fig. 23. Realized common-mode inductors.

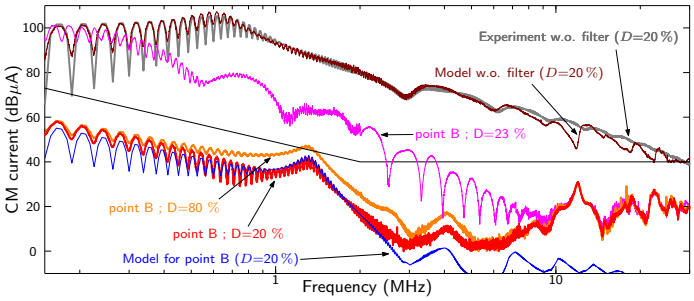

Fig. 24. CM current spectrum without filter and with the realized inductor at point B.

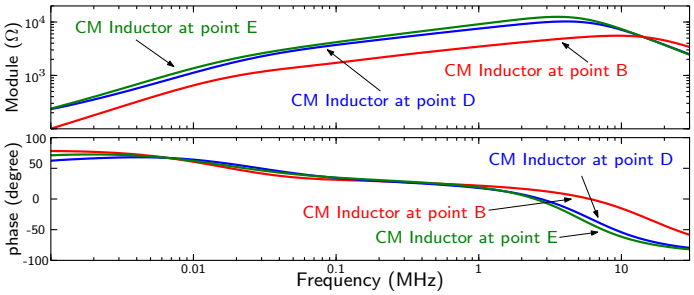

Fig. 25. Common-mode impedances of the realized common-mode inductors.

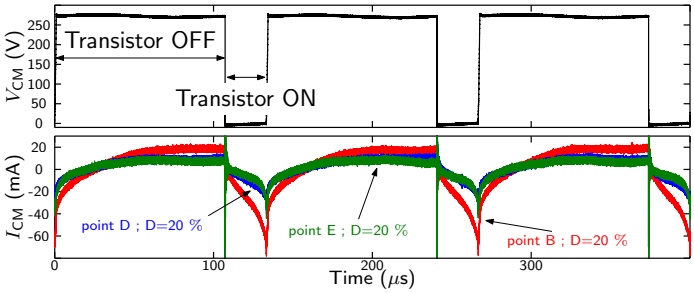

Fig. 26. CM current waveforms with the realized CM inductors (D = 20 %).

used 28-meter long shielded cable has a high CM capacitance (about 16 nF) compared the converter CM capacitance. Then, its CM impedance presented in Fig. 8 and taken into account in the used model, masks almost all the imperfections caused by the DC-DC converter.

The first realized inductor at point B, near the minimal required inductance value L_{LF}^{min}, was designed by ensuring the non saturation constraint NS (wire spacing naturally higher than s and is equal to about 2.16 mm). The expected CM current calculated from the model is shown in blue line in Fig. 24: it should allow to respect the normative constraint with just a slight margin at the functioning point with 20 % duty cycle. Measurements (red line) confirm the predicted level up to a few megahertz where the model is no longer valid due to parasitic high-frequency effects (such as inter-turn capacitance) not being taken into account. Still, even in high frequencies (beyond 10 MHz), the EMC standard is also respected due to the high impedance of the inductor offered by the used nanocrystalline material as shown in red line in Fig. 25.

The high CM current in low frequencies impacts the magnetic core and generates a nonlinearity in the CM current waveform as shown in Fig. 26 (red line), which indicates that the CM inductor is near saturation. For this reason, the calculated CM current in Fig 24 (blue line) is actually slightly lower than experiments in low frequencies, indicating that inductance value starts to be impacted by the high values of the low frequencies CM current. In fact, changing slightly the duty cycle to 23 % causes a complete saturation of the magnetic core due to the increase of magnetic flux ripple at the switching frequency when the duty cycle approaches 50 %. As a consequence, the designed filter attenuation is lost and the HF CM noise largely exceeds the standard limit as shown in Fig. 24 (pink line).

Actually, increasing the duty cycle not only increases the CM current level, but also the differential current due to higher transferred power to the R-L load. Thus, it may be questionned whether this current is the cause of local core saturation because of the existing inductor leakage flux [13]. To prove that the saturation phenomena, shown at 23 % duty cycle in Fig. 24, is directly related to the CM flux ripple around the switching frequency, another test is performed at 80 % duty cycle with Vdc always equal to 540 V. This functioning point increases the DM current by a factor of four compared with the initial 20 % duty cycle, while theoretically keeping the same CM current ripple. As shown in Fig. 24 (orange line), the used

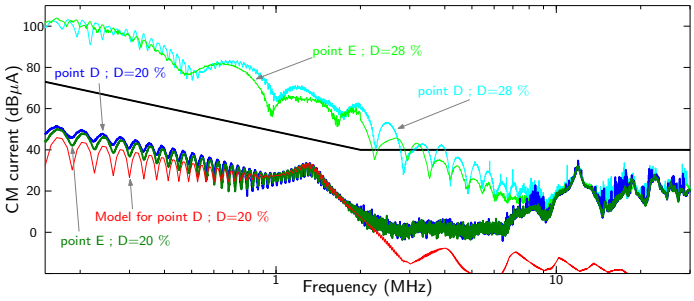

Fig. 27. CM current spectrum with the realized inductors at points D and E.

magnetic core is not saturated anymore and the measured CM current drops back to almost its initial level. In fact, when $D = 80\,\%$, CM current level is slightly higher in the megahertz range compared to the result when $D = 20\,\%$ because of the reduction of the transistor rise time (at turn-off) when it commutes higher differential currents, which induces more CM noise. Thus, this result confirms the preceding analysis and the validity of the proposed approach taking into account CM-current-related saturation issues of the magnetic core.

The second realized inductor at point D, is the best inductance value L_{LF}^{best} that minimizes the optimal volume. It is designed by ensuring both the non saturation NS and the single layer SL constraints, which means that the maximum magnetic field H_{max} is equal to H_{sat} and the number of turns N_{opt} is maximized to cover all the core window (wire spacing is equal to s in this case). Its best volume is equal to $3.71\,cm^3$, only $23\,\%$ of the optimal volume at the minimal required inductance value L_{LF}^{min}. Its high CM impedance compared to the first designed CM inductor (blue line in Fig. 25) provides a large margin for the CM current to respect the normative constraint at $20\,\%$ duty cycle as shown in Fig. 27 (blue line). The maximum CM current with this inductor is reduced comparing to the first one as shown in Fig. 26 (blue line). However, the number of turns is higher and the nonlinearity is still observed in the CM current waveform, which confirms that this inductor is designed close to saturation ($H_{max} = H_{sat}$) by ensuring the NS constraint, as well as by the SL constraint, which induce a slight difference between the predicted and the measured current in low frequencies as well as for the point B case. In fact, just increasing the duty cycle up to $28\,\%$ saturates the magnetic material as shown in Fig. 27 (light blue line).

The third realized inductor at point E, has almost the same inductance value and the same volume as the second one at point D (only a difference of $1.2\,\%$ on the inductance value and less than $1\,\%$ on the inductor volume). However, geometrical parameters are completely different (lower height and higher external radius and number of turns). The CM performances of the realized filter is almost the same as the last one as shown in Fig. 26 and Fig. 27 (green and light green lines). In fact, it respects the normative constraint at $20\,\%$ of duty cycle and saturates when the duty cycle equals $28\,\%$, exactly the same as the realised inductor at point D.

The third realised inductor (at point E) has a number of turns higher than its equivalent at point D. Then, at first glance, it may seems that it has more parasitic capacitance than the other one. However, as shown in Fig. 25, the two inductors at points D and E have almost the same impedance value in high frequencies, which proves that the filters have the same performances in all the frequency range between $150\,kHz$ and $30\,MHz$.

Thus, these results confirm that the best inductor volume can be obtained with different geometries, with keeping the same filter performance in the whole frequency range defined by the EMC standard, which provides an extra degree of freedom to designers while integrating the filter in the conversion chain.

Finally, a thermal evaluation has been performed on the two low-volume inductors (points D and E) for $20\,\%$ duty cycle, using and IR thermal camera and a thermocouple, at $25\,°C$ ambient temperature. In steady state, the measured temperature on the core external surface was $56\,°C$ for the best inductor (point D) and $60.5\,°C$ for the near-best one (point E). Even though more torough thermal study is required to fully analyse the CM inductors thermal behavior, these rough measurements are consistent with the theoretical calculations of the core surfaces, as Fig. 21(b) shows that the inductor at point D benefits from larger thermal exchange surface with ambient air than the inductor at point E.

V. Conclusion

In this paper, a new optimization method of the common-mode coupled inductor for EMI filters is proposed. The calculation of an LC filter parameters taking into account the input/output terminal impedances in addition the magnetic material complex permeability is detailed. The proposed minimization tool of the CM inductor volume takes into account saturation issues of the magnetic material which may considerably increase the inductor volume. Applying this method to a given power electronic system shows that the optimal (best) inductor volume is not always obtained at the minimal required inductance value to meet the EMC standard. In fact, increasing the inductance value up to a best value reduces the low frequency common-mode current impact on the magnetic material behaviour. Generally, when the design of CM inductor is made by ensuring the non saturation constraint, increasing inductance value up to the best value may considerably decrease the volume of the core in addition to further enhancing filter attenuation. The obtained results show that nearly-best inductor volume can be obtained with different shape factors concerning the core geometrical parameters which provides an important degree of freedom to designers while integrating the filter in the electrical system. In a next step, CM inductor volume will be optimized by including the optimization of the inter-turn capacitance value in addition to the choice of the magnetic material and the thermal constraint. Also, a global optimization of the CM filter taking into capacitor characteristics is one of the perspectives related to the proposed method.

Acknowledgment

This work has been achieved within the framework of CE2I project (Convertisseur d'Energie Intégré Intelligent). CE2I is co-financed by European Union with the financial support of

European Regional Development Fund (ERDF), French state and the French Region of Hauts-de-France.

REFERENCES

[1] B. Touré, J. L. Schanen, L. Gerbaud, T. Meynard, J. Roudet, and R. Ruelland, "EMC Modeling of Drives for Aircraft Applications: Modeling Process, EMI Filter Optimization, and Technological Choice," *IEEE Transactions on Power Electronics*, vol. 28, no. 3, pp. 1145–1156, March 2013.

[2] D. Boroyevich, X. Zhang, H. Bishinoi, R. Burgos, P. Mattavelli, and F. Wang, "Conducted EMI and systems integration," in *Integrated Power Systems (CIPS), 2014 8th International Conference on*, Feb 2014, pp. 1–14.

[3] B. Zaidi, A. Videt, and N. Idir, "Design Method for the Minimization of CM Inductor Volume with Consideration of Core Saturation in EMI Filters," in *PCIM Europe 2017; International Exhibition and Conference for Power Electronics, Intelligent Motion, Renewable Energy and Energy Management*, May 2017, pp. 1–8.

[4] F. Luo, S. Wang, F. Wang, D. Boroyevich, N. Gazel, Y. Kang, and A. C. Baisden, "Analysis of CM Volt-Second Influence on CM Inductor Saturation and Design for Input EMI Filters in Three-Phase DC-Fed Motor Drive Systems," *IEEE Transactions on Power Electronics*, vol. 25, no. 7, pp. 1905–1914, July 2010.

[5] B. Zaidi, A. Videt, and N. Idir, "Design method for the minimization of common-mode inductor volume taking into account saturation issues in EMI filters for variable duty cycle applications," in *2017 19th European Conference on Power Electronics and Applications (EPE'17 ECCE Europe)*, Sept 2017, pp. P.1–P.10.

[6] L. Fang, D. Boroyevich, P. Mattevelli, and N. Gazel, "A comprehensive design for high power density common mode EMI inductor," in *2011 IEEE Energy Conversion Congress and Exposition*, Sept 2011, pp. 1861–1867.

[7] B. Zaidi, A. Videt, and N. Idir, "Influence of switching frequency and saturation of the magnetic material on the volume of common-mode inductors used in power converter EMI filters," in *2017 IEEE Energy Conversion Congress and Exposition (ECCE)*, Oct 2017, pp. 887–894.

[8] G. Ala, G. C. Giaconia, G. Giglia, M. C. D. Piazza, M. Luna, G. Vitale, and P. Zanchetta, "Computer aided optimal design of high power density EMI filters," in *2016 IEEE 16th International Conference on Environment and Electrical Engineering (EEEIC)*, June 2016, pp. 1–6.

[9] Y. Maillet, R. Lai, S. Wang, F. Wang, R. Burgos, and D. Boroyevich, "High-Density EMI Filter Design for DC-Fed Motor Drives," *IEEE Transactions on Power Electronics*, vol. 25, no. 5, pp. 1163–1172, May 2010.

[10] F.-Y. Shih, D. Y. Chen, Y.-P. Wu, and Y.-T. Chen, "A procedure for designing EMI filters for AC line applications," *IEEE Transactions on Power Electronics*, vol. 11, no. 1, pp. 170–181, Jan 1996.

[11] C. Cuellar and N. Idir, "EMI filter design methodology taking into account the static converter impedance," in *2014 16th European Conference on Power Electronics and Applications*, Aug 2014, pp. 1–10.

[12] T. McLyman, "Transformer and Inductor Design Handbook, third edition, revised and expanded," *New York, Marcel Dekker*, 2004.

[13] M. L. Heldwein, L. Dalessandro, and J. W. Kolar, "The Three-Phase Common-Mode Inductor: Modeling and Design Issues," *IEEE Transactions on Industrial Electronics*, vol. 58, no. 8, pp. 3264–3274, Aug 2011.

[14] D. K. Saini, A. Ayachit, A. Reatti, and M. K. Kazimierczuk, "Analysis and Design of Choke Inductors for Switched-Mode Power Inverters," *IEEE Transactions on Industrial Electronics*, vol. 65, no. 3, pp. 2234–2244, March 2018.

[15] A. Muetze and C. R. Sullivan, "Simplified Design of Common-Mode Chokes for Reduction of Motor Ground Currents in Inverter Drives," *IEEE Transactions on Industry Applications*, vol. 47, no. 6, pp. 2570–2577, Nov 2011.

[16] M. Delhommais, G. Dadanema, Y. Avenas, F. Costa, J. L. Schanen, and C. Vollaire, "Design by optimization of power electronics converter including EMC constraints," in *2016 International Symposium on Electromagnetic Compatibility - EMC EUROPE*, Sept 2016, pp. 182–187.

[17] D. O. Boillat, F. Krismer, and J. W. Kolar, "EMI Filter Volume Minimization of a Three-Phase, Three-Level T-Type PWM Converter System," *IEEE Transactions on Power Electronics*, vol. 32, no. 4, pp. 2473–2480, April 2017.

[18] R. Wang, D. Boroyevich, H. F. Blanchette, and P. Mattavelli, "High power density EMI filter design with consideration of self-parasitic," in *2012 Twenty-Seventh Annual IEEE Applied Power Electronics Conference and Exposition (APEC)*, Feb 2012, pp. 2285–2289.

Bilel ZAIDI received the Diploma in electrical engineering from Ecole Nationale Superieure d'Ingenieurs de Tunis, Tunisia in 2014, and the Master degree in automatic and applications from Ecole Nationale Superieure d'Ingenieurs de Poitiers, France in 2015. He is currently working toward the Ph.D. degree in electrical engineering at the L2EP laboratory, University of Lille, France. His research interests include passive EMI filters design and ferromagnetic materials used in power electronics.

Arnaud VIDET (M'09) received the Ph.D degree in electrical engineering from Ecole Centrale de Lille, France, in 2008, and joined Schneider Toshiba Inverter, Pacy-sur-Eure, France, where his research focused on motor drive converter topologies and modulation strategies. Since 2010, he is Associate Professor with the L2EP laboratory, University of Lille, France. His research interests include power devices and electromagnetic compatibility issues in power converters.

Nadir IDIR (M'93) received the Ph.D. degree electrical engineering from the University of Lille, France, in 1993. He is a Full Professor with IUT A, University of Lille , Lille, France, where he teaches power electronics and electromagnetic compatibility. Since 1993, he has been with the Laboratory of Electrical Engineering and Power Electronics. His research interests include design methodologies for high-frequency switching converters, power devices (SiC and GaN), electromagnetic compatibility of the static converters, HF modeling of the passive components, and electromagnetic interference filter design methodologies.